
# Internal Oxidation of a Fe-Cr Binary Alloy at 700-900 degrees C: The Role of Hydrogen and Water Vapor

Oxidation of Metals (2022) 98:273–289
https://doi.org/10.1007/s11085-022-10121-7

ORIGINAL PAPER

# Internal Oxidation of a Fe–Cr Binary Alloy at 700–900 °C: The Role of Hydrogen and Water Vapor

**Anton Chyrkin[1] · Camilla Cossu[1] · Jan-Erik Svensson[1] · Jan Froitzheim[1]**

Received: 19 January 2022 / Revised: 24 May 2022 / Accepted: 1 June 2022 /
Published online: 28 June 2022


## Abstract

Internal oxidation of Fe–2.25Cr has been studied in Fe/FeO Rhines pack (RP) and $H_2/H_2O$ gas mixtures at 700–900 °C. A novel exposure technique allowing RP experiments in dual atmosphere conditions was developed. No measurable effect of hydrogen on lattice oxygen permeability in ferrite could be detected: neither in single nor in dual atmosphere conditions. The $H_2/H_2O$ atmosphere was found to induce stronger oxidation attack at alloy grain boundaries resulting in a morphology similar to intergranular stress corrosion cracking often reported in nuclear technology. The intergranular oxidation attack was demonstrated to be independent of the dual atmosphere effect, i.e., hydrogen dissolved in the alloy.

**Keywords** Internal oxidation · Oxygen permeability · Hydrogen · Dual atmosphere effect · Intergranular oxidation attack · SOFC

## Introduction

Due to increasing awareness on climate change, "green energy" technologies are in great demand. Solid oxide fuel cells (SOFCs) [1] provide electricity with a high efficiency while the reverse process, solid oxide electrolysis cell (SOEC) [2, 3] allows to produce hydrogen or the synthetic fuels required to transform into a low carbon society. In both cases, the essential building block, a stack, consists of many individual cells that are connected in series[4–6]. Between the cells, metallic interconnects are placed. The metal sheets, usually 0.2–0.5 mm thick, comprise ferritic stainless steel [6, 7] that once coated exhibit low Cr(VI)- evaporation [8, 9] and usually provide acceptable corrosion protection at the operating temperature of 600–900 °C. The corrosion of interconnects differs from most other high-temperature applications that one side of the

✉ Jan Froitzheim
jan.froitzheim@chalmers.se

[1] Department of Chemistry and Chemical Engineering, Chalmers University of Technology, Gothenburg, Sweden

metal sheet is exposed to air or an oxygen-rich gas while the other side is exposed to a $H_2/H_2O$ environment potentially mixed with CO, $CO_2$ and hydrocarbons.

Work by Yang et al. [10] showed that oxidation under such dual atmosphere conditions differs from oxidation in single atmosphere, i.e., the same atmosphere on both sides. This finding spurred a lot of work on this field resulting in somewhat contradictory results [11–17]. Nevertheless, it is nowadays firmly established that the dual atmosphere effect is real and recent work by Gunduz et al. [17, 18] explains how different parameters influence the effect and thus shedding light on the discrepancies reported in the literature. Although the exact mechanism is still debated, authors agree upon that hydrogen from the hydrogen rich side diffuses through the metal and negatively affects air-side oxidation.

Apart from dual atmosphere effect, water vapor alone is well known to deteriorate performance of chromia-forming alloys, especially ferritic steels [19–23], the detrimental effect being generally attributed to reactive Cr(VI)-evaporation [24–27], modification of transport properties of the $Cr_2O_3$ scale [28, 29], preferential adsorption of $H_2O$ [30] and dissolution of hydrogen in the metal [19, 31–33]. Decades of research on the role of hydrogen/humidity on protectiveness of chromia scales resulted in a number of commonly reported mechanisms: (i) $H_2O$ promoting $O_2$ transport in the voids of the oxide bridging them [34]; (ii) hydrogen modifying the lattice point defect structure of $Cr_2O_3$ via incorporation of $H^+$ and/or $HO^-$ [28]; (iii) formation of volatile species such as Fe-hydroxides [34, 35] or Cr-oxyhydroxides [24]; (iv) preferential adsorption of water molecules [30]; (v) dissolution of hydrogen increasing oxygen permeability [19, 36–40].

Several authors recently questioned the effect of water vapor and hydrogen on the oxygen permeability based on internal oxidation experiments in Fe–Ni–Cr [41–43] and Pd–Cr [44, 45] alloys. Some of the aforementioned studies were carried out at temperatures that substantially exceed the application range of SOFC/SOEC, 600–800 °C, while the works by Gunduz et al. [17, 18] and Alnegren et al. [13, 14] have shown that the dual atmosphere effect intensifies with decreasing temperature. Therefore, extrapolating the conclusions from [41–43] to lower temperatures must be done with utmost precaution.

In the present study, the effect of hydrogen on internal oxidation in single and dual atmosphere conditions has been studied. Oxygen permeabilities were measured for a Fe–2.25Cr model alloy exposed in Fe/FeO Rhines pack and Ar–$H_2$–$H_2O$ gas mixtures at 700–900 °C as well as in dual atmosphere conditions, i.e., Fe/FeO Rhines pack versus $H_2/H_2O$, at 700 °C. The obtained internal oxidation zones (IOZ) were characterized with light optical microscopy and SEM. The IOZ morphologies were discussed as a function of temperature, the presence of hydrogen in the system and its source.

## Experimental Procedures

### Material

The binary model alloy Fe–2.25Cr (wt.%), simulating a low-grade steel, was supplied by Sandvik Materials Technology AB. The chemical composition of the alloy is given

in Table 1. The alloy has an average gain size of 50 µm; more information on the same alloy batch can be found in [20]. For the single atmosphere RP and $H_2/H_2O$ exposures, test coupons measuring 10 × 10 × 2 mm were machined from a hot-extruded bar 25 mm in OD. The circular specimens for the dual atmosphere experiments were cut from the same bar. The 0.5-mm-thick discs 21 mm in diameter were ground with SiC paper to 0.2 mm. All specimens were polished with diamond paste to 0.25-µm surface finish, subsequently cleaned with acetone and ethanol in an ultrasonic bath and dried with pressurized air prior to exposure.

### Rhines Pack Exposures

The Fe/FeO mixture was prepared from an iron powder supplied by BDH Chemicals Ltd (England) adopting a modified procedure described by Prillieux et al. [42]. The iron powder was oxidized in Ar–5$H_2$%–3%$H_2O$ at 800 °C for 24 h. The degreased alloy coupons were sealed together with the Fe/FeO mixture in a 16 mm OD quartz tube either under vacuum ($10^{-5}$ mbar) or a shielding atmosphere of Ar. In the latter case, the residual gas pressure was set to achieve 1 bar at the exposure temperature. Selected exposures were carried out with RP sealed at 0.3, 0.6 and 0.9 bar of Ar–5%$H_2$ to achieve 1, 2 and 3 bar, respectively, at 700 °C. No differences in IOZ morphology and depth between vacuum and Ar-shielded RP exposures were established. The sealed quartz capsules were introduced into the hot zone of a tube furnace, removed at the end of the exposure and quenched in water. The specimens were exposed at 700, 800, 850 and 900 °C for up to 192 h.

### $H_2/H_2O$ Exposures

The $H_2/H_2O$ exposures were performed in a quartz tube in a horizontal furnace. The Ar-5%$H_2$ gas mixture supplied by Linde Gas was bubbled through a humidifier (Fig. 1b) kept at a certain temperature to obtain the level of $H_2O$ corresponding to the Fe/FeO equilibrium (Table 2). Unlike the RP exposures, the specimens were introduced into a cold furnace, flushed with the dry Ar–5%$H_2$ gas for 1 h and heated at 10 K $min^{-1}$ per minute to reach exposure temperature °C. The humidification was turned on once the furnace reached the desired temperature. The cooling rate was 10 K $min^{-1}$ as well. The gas flow rate was set at 200 ml $min^{-1}$. The exposure durations were the same as for the RP exposures.

### Two-Step Exposures

To better understand the effect of hydrogen on the internal oxidation morphology at 700 °C, four two-step exposures alternating the $H_2/H_2O$ and RP exposures were carried

**Table 1** Chemical composition of the binary Fe–Cr alloy in wt.%

| Fe | Cr | Al | Ti | Mn | Mo | Ni | Co | C | S |
|---|---|---|---|---|---|---|---|---|---|
| Bal | 2.26 | 0.02 | 0.02 | 0.02 | 0.01 | 0.01 | 0.01 | 0.005 | 0.005 |

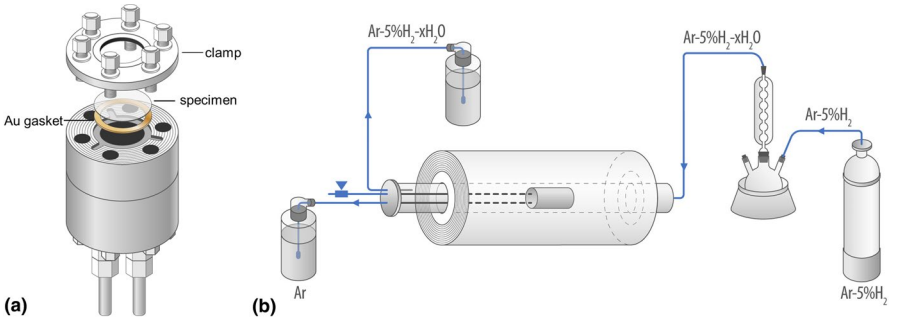


**Fig. 1** Schematic of the specimen holder designed for Rhines pack (RP) dual exposures: **a** reaction chamber, **b** furnace setup providing RP atmosphere inside and $H_2/H_2O$ environment outside the reaction chamber

**Table 2** Partial pressures of oxygen, hydrogen and water vapor prevailing in exposures at the Fe/FeO decomposition level at 700–900 °C calculated using standard enthalpies and entropies from [57]

| Exposure temperature | $pO_2$/bar Fe/FeO | $pH_2$/mbar | $pH_2O$/mbar | $pO_2$/bar $H_2/H_2O$ | Dew point (°C) |
|---|---|---|---|---|---|
| 700 | $2.5\times10^{-22}$ | 49 | 17 | $2.3\times10^{-22}$ | 15,1 |
| 800 | $1.1\times10^{-19}$ | 49 | 22 | $1.1\times10^{-19}$ | 19,0 |
| 850 | $1.6\times10^{-18}$ | 49 | 24 | $1.5\times10^{-18}$ | 20,5 |
| 900 | $1.7\times10^{-17}$ | 49 | 26 | $1.7\times10^{-17}$ | 21,7 |

out. In the first step, two pairs of alloy coupons were exposed for 72 h in parallel in $H_2/H_2O$ and RP at 700 °C as described above. In the second step, two specimens from each pair were swapped, while the two other specimens were further exposed in the initial conditions for another 120 h. As a result, two specimens in this experiment were exposed only to $H_2/H_2O$ and RP with an intermediate cooling step. The discontinuously exposed specimens served as a reference. The other two specimens were consecutively exposed to both atmospheres: $H_2/H_2O$—RP and RP—$H_2/H_2O$.

## Dual Atmosphere Exposure

To simulate the dual atmosphere between Fe/FeO and $H_2/H_2O$, a special specimen holder was designed. As demonstrated in Fig. 1a, a semi-hollow cylindric reactor head, 40 mm OD, with an inner chamber, 16 mm ID, was produced from 253 MA steel and welded to 6-mm 316-L steel tubes. The inner chamber was stuffed with quartz wool and filled with 2 g of Fe/FeO powder. The circular alloy specimens were clamped with a steel clamping ring. Gold gaskets were used to seal tightly the specimen to the sample holder. Once the specimen was mounted, the inner chamber was purged with Ar at the rate of 50 ml $min^{-1}$ for 1 h. After the purge, the gas inlet was closed, while the gas level in the wash-bottle at the outlet was controlled to be stable proving thus the gas tightness of the system (Fig. 1b). The closed

sample holder was placed in a 42 mm ID quartz tube in a horizontal furnace. The quartz tube was tightly closed on one side with a steel flange welded to the connecting tubes and supplied with an O-ring and then flushed with Ar–5%$H_2$ for 1 h at room temperature. While heated to the exposure temperature, the specimen holder released the expanding Ar from the RP chamber into the wash bottle. At the test temperature, the inner pressure was maintained at 1 bar. The heating and cooling rate was 10 K $min^{-1}$. The humidification was switched on filling thus the quartz tube with the Ar-$H_2$-$H_2O$ mixture (see gas compositions in Table 2) once the exposure temperature was reached. The flow rate of Ar–$H_2$–$H_2O$ in the quartz tube was 100 ml $min^{-1}$. The dual atmosphere experiment was run at 700 °C for 192 h.

### Microstructural Analyses

The exposed specimens were sectioned, hot-mounted, subsequently ground with SiC paper to 2500 grits and polished to 0.25-µm surface finish. The final ion etching step was performed using the Gatan PECS II System. Some cross sections, especially the dual atmosphere specimens, were prepared employing the broad-ion beam (BIB) technique using a Leica EM TIC 3X. FEI Quanta 200 ESEM and JEOL JSM-7800F Prime electron microscopes equipped with an energy-dispersive X-ray spectrometer (EDS) were used for post-exposure analyses.

## Results

Figure 2 shows the BSE images of IOZs in Fe–2.25Cr exposed for 72 h at 850 °C in $H_2$/$H_2O$ and in RP. The distinct and uniform IOZs have essentially the same depth of $63 \pm 2$ µm ($H_2$/$H_2O$) and $62 \pm 2$ µm (RP), respectively. As reported in numerous studies [38, 40, 42], the IOZ precipitates are iron-chromium spinel $FeCr_2O_4$. The grain boundaries in both IOZs are densely filled with the spinel. Prillieux et al. [42] found precipitates of $Cr_2O_3$ close to the reaction front after exposures at 1100 and 1150 °C. In the present study, the crystal structure of the oxide precipitates could not be resolved in the IOZs. Minor traces of FeO can be seen on the surface in the RP specimen (Fig. 2b).

Figure 3 shows the BSE images of IOZs in Fe–2.25Cr exposed for 192 h at 700 °C in $H_2$/$H_2O$ and in RP. Most importantly, the IOZs reflecting the oxygen permeation in the lattice are of the same depth of $10.5 \pm 1$ µm ($H_2$/$H_2O$) and $11 \pm 1$ µm (RP), respectively (Fig. 3c, d). However, unlike the uniform IOZs at 850 °C and 900 °C (not shown here), the IOZ in $H_2$/$H_2O$ (Fig. 3a) revealed a stronger oxidation attack at the alloy grain boundaries which will be termed hereafter GB tail. At the same time, no such GB tail has been observed in the RP specimen (Fig. 3b). The tails only slightly protrude at the GBs beyond the IOZ. The IOZ measurements are summarized in Table 3.

The width of a uniform IOZ is plotted in Fig. 4 as a function of $(t)^{1/2}$. The internal oxidation kinetics obeys a parabolic time-law and is diffusion controlled. The data points are in very good agreement at all temperatures, and no significant difference

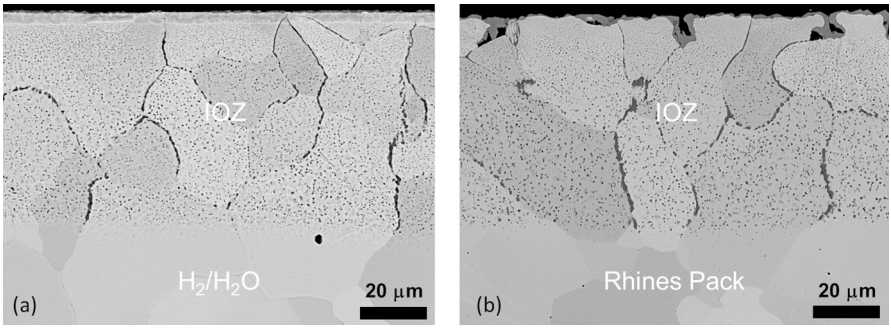


**Fig. 2** BSE images of BIB cross-sectioned alloy specimens exposed for 72 h at 850 °C in **a** $H_2/H_2O$ and **b** Fe/FeO RP

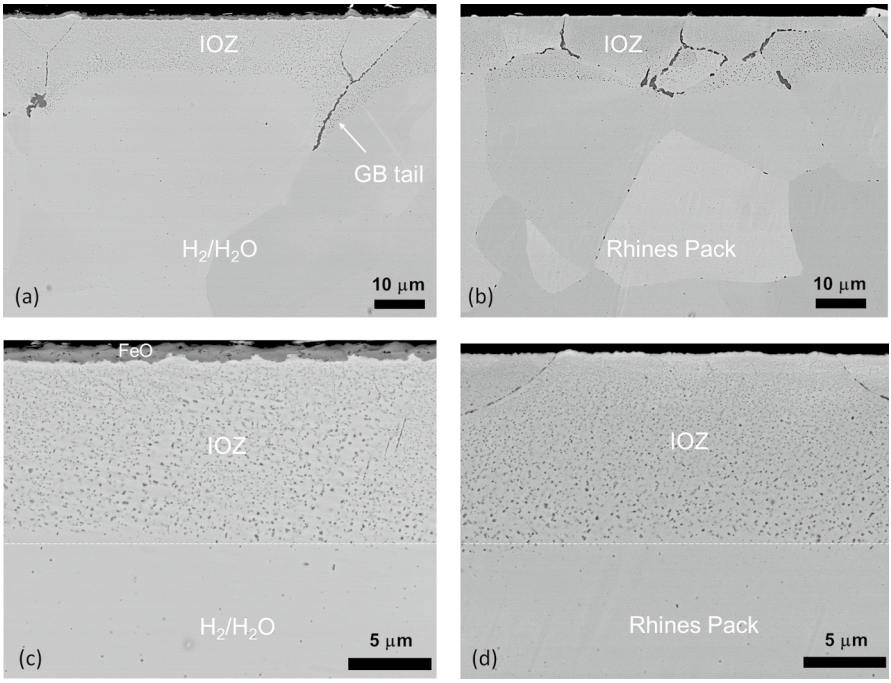


**Fig. 3** BSE images of BIB cross-sectioned alloy specimens exposed for 192 h at 700 °C in **a**, **c** $H_2/H_2O$ and **b**, **d** Fe/FeO RP.**c**, **d** demonstrate bulk internal oxidation zone (IOZ)

between IOZs grown in $H_2/H_2O$ and RP could be observed. The length of the GB tails measured from the alloy surface is also plotted in Fig. 4. Like the bulk IOZ, the GB tail growth kinetics is diffusion controlled.

The apparent oxygen permeabilities were calculated using Wagner's analysis of internal oxidation taking into account counter-diffusion of Cr and neglecting volume change effects in a diluted Fe–Cr alloy as described in Refs. [46, 47] and plotted

**Table 3** Bulk IOZ width, $X_{IOZ}$, and intergranular oxidation depth, $X_{IG}$, in various Fe–2.25Cr specimens exposed for 192 h at 700 °C

| Environment | $X_{IOZ}$ (μm) | $X_{IG}$ (μm) |
|---|---|---|
| Isothermal exposures | | |
| Fe/FeO (RP) | 10.9 | 14.8 |
| $H_2/H_2O$ | 11.0 | 32.2 |
| Dual atmosphere exposure | | |
| RP side | 11.0 | 12.0 |
| $H_2/H_2O$ side | 10.6 | 29.5 |
| Pressurized exposures | | |
| RP + 1 bar Ar − 5%$H_2$ | 10.2 | 12.0 |
| RP + 2 bar Ar − 5%$H_2$ | 11.0 | 15.1 |
| RP + 3 bar Ar − 5%$H_2$ | 11.3 | 17.7 |
| Alternating exposures | | |
| 72 h RP + 120 h RP | 10.4 | 13.1 |
| 72 h $H_2/H_2O$ + 120 h $H_2/H_2O$ | 10.6 | 31.7 |
| 72 h RP + 120 h $H_2/H_2O$ | 10.5 | 20.8 |
| 72 h $H_2/H_2O$ + 120 h RP | 10.4 | 19.5 |

The average IOZ width in all experiments (192 h at 700 °C) is 10.6 ± 1 μm

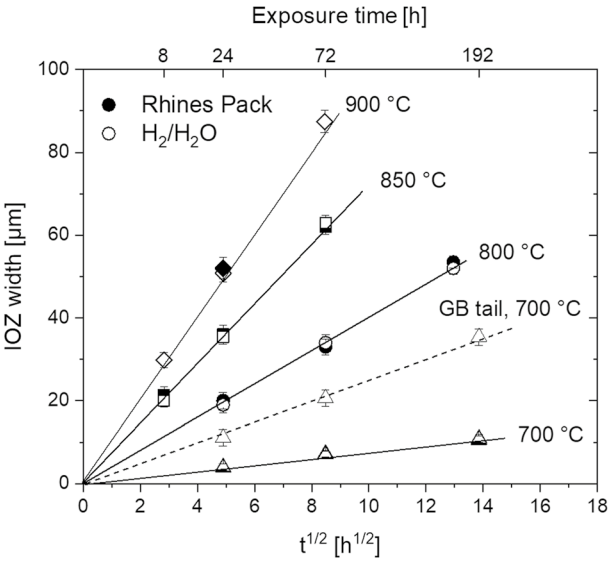


**Fig. 4** Kinetics of internal oxidation in Fe–2.25Cr in RP (full symbols) and $H_2/H_2O$ (empty symbols)

together with the available literature data in Fig. 5. The obtained data showed a very good agreement with the literature for the absolute $N_O^{(s)}D_O$ values as well as activation energy of 200 kJ mole$^{-1}$. No effect of hydrogen can be deduced from the obtained results.

Figure 6 shows the BSE micrographs of the two sides of the 0.2-mm-thick specimen after 192 h of exposure in dual atmosphere at 700 °C. As the $pO_2$ of the Ar–$H_2$–$H_2O$ gas was slightly higher than the dissociation oxygen partial pressure for FeO ($2.5 \times 10^{-22}$ bar), a thin layer of wüstite can be seen on the surface of the $H_2/H_2O$ side. On the other hand, the surface of the RP side is completely free of FeO. Notably, the bulk IOZs are equally thick on both sides ($10.7 \pm 1$ µm) and match very well the IOZs in the single specimens (Fig. 3c, d). Additionally, the characteristic IOZ morphologies were recreated in the dual atmosphere exposure: the GB tail appeared on the $H_2/H_2O$ side (Fig. 6a) but not on the RP side (Fig. 6a).

Figure 7 demonstrates IOZs grown in Fe–2.25Cr after RP exposures under different pressures of Ar–5%$H_2$ for 192 h in at 700 °C. A specimen exposed to "dry" RP, i.e., sealed under vacuum, is included in Fig. 7a as a reference. Irrespective of the used pressure of Ar–5%$H_2$, these experiments revealed no effect of ambient $H_2$ on the bulk IOZ width. Furthermore, only a weak $pH_2$ dependence of the intergranular penetration can be derived from Figs. 7 and 8 summarizing the measurements (see also Table 3).

Figure 9 shows the results of the two-step exposures. First, the reference specimens were found to form exactly the same IOZs as those after isothermal experiments compare Figs. 3a, 9a and Figs. 3b, 9b, respectively. Both IOZ morphologies and the bulk IOZ width matched very well. The two-step specimens with changed atmosphere demonstrated an intermediate IOZ morphology between $H_2/H_2O$ and RP. The bulk IOZs measuring $10.4 \pm 1$ µm for the $H_2/H_2O$—RP specimen and $10.6 \pm 1$ µm for the RP—$H_2/H_2O$ specimen agree with all measurements above. The GB tail appears shorter in the two-step specimens indicating a direct correlation between the internal GB oxidation attack and the time of exposure to $H_2/H_2O$.

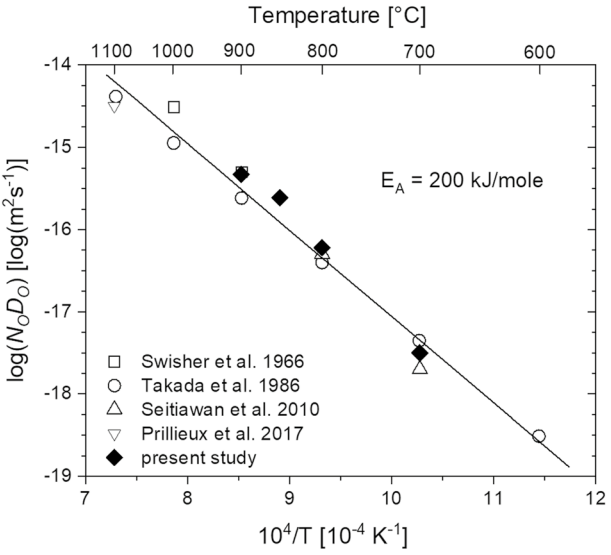


**Fig. 5** Averaged oxygen permeabilities in Fe–2.25Cr determined from internal oxidation experiments in RP and $H_2/H_2O$ (full symbols) in this study compared with literature data (empty symbols)

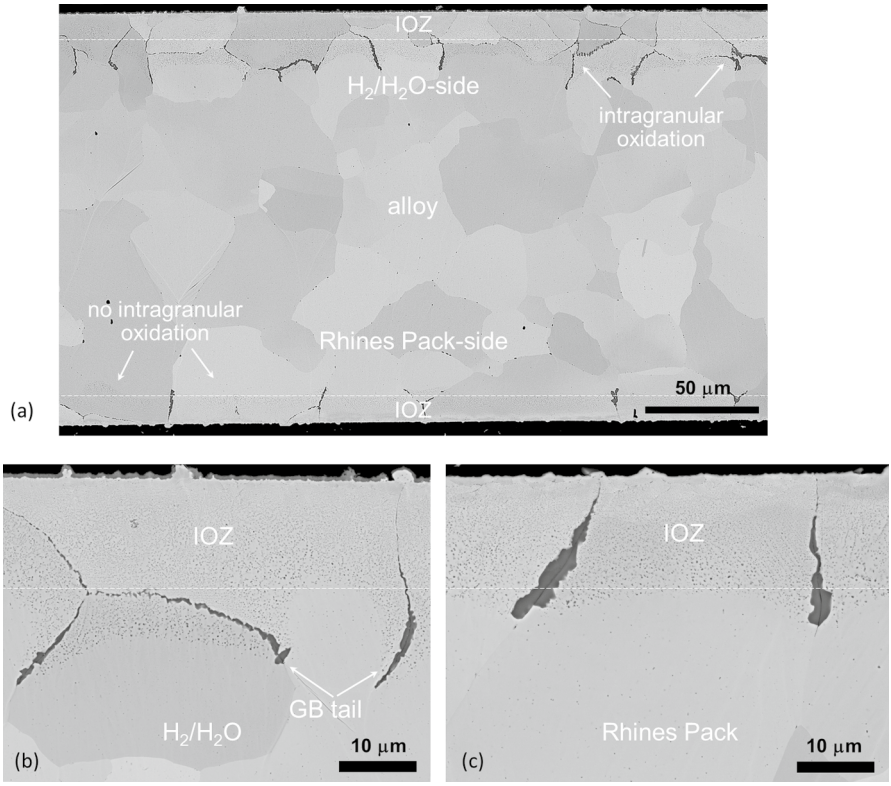


**Fig. 6** BSE images of internal oxidation zones IOZ in BIB cross-sectioned Fe–2.25Cr specimen exposed for 192 h at 700 °C in dual atmosphere conditions: **a** Overview, **b** $H_2/H_2O$ side, **c** Rhines pack side

## Discussion

### Effect of Hydrogen on Lattice Oxygen Permeability

The idea of hydrogen increasing oxygen permeability in iron and in alloys in general was for the first time postulated in [36]. In these studies, a binary borderline model alloy Fe-10Cr oxidized completely internally in Ar–4%$H_2$–2%$H_2O$ while forming a mixed duplex, external and internal, oxide scale in Ar–20%$O_2$ at 900 °C. Hydrogen was thus believed to promote internal oxidation and, hence, increase oxygen permeability, $N_O^{(s)}D_O$. This hypothesis was further supported by experimental evidence from the studies of internal oxidation in diluted Fe–Cr at 700–800 °C in an evacuated environment equilibrated with Fe/FeO and some residual hydrogen pressure [39, 40]. The IOZs in "humid" atmospheres were found to be broader with respect to those in the "dry" ones. However, the latter effect was rather weak, never exceed 20% and could be alternatively interpreted as the effect of the precipitate morphology in the IOZ.

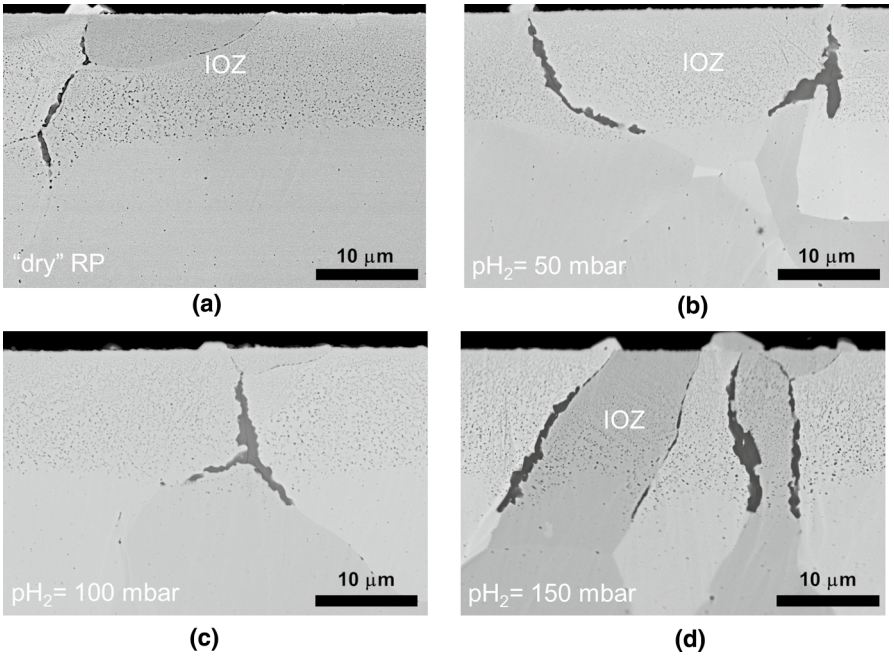


**Fig. 7** Effect of external hydrogen partial pressure on IOZ morphology in Fe–2.25C exposed for 192 h at 700 °C in Fe/FeO RP under various pressures of Ar-5%$H_2$

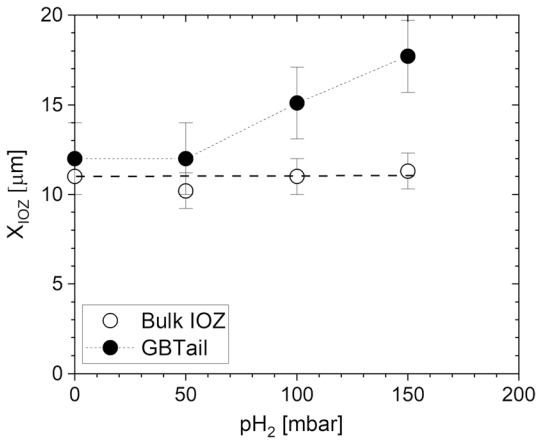


**Fig. 8** Effect of partial pressure of $H_2$ equilibrated with Fe/FeO RP in a sealed quartz capsule on bulk IOZ (open symbols) and GB tail depth (full symbols) after 192 h at 700 °C

Subsequently, a systematic study of internal oxidation in Fe–Ni–Cr alloys in a broad composition range was undertaken in Fe/FeO, $H_2/H_2O$, and $CO/CO_2$ [41–43, 48]. The abundant and systematic evidence demonstrated no measurable effect of hydrogen or carbon on lattice oxygen permeability at 1000–1150 °C. Further evidence of no effect of hydrogen on internal oxidation can be found in other studies in which IOZs of $Al_2O_3$

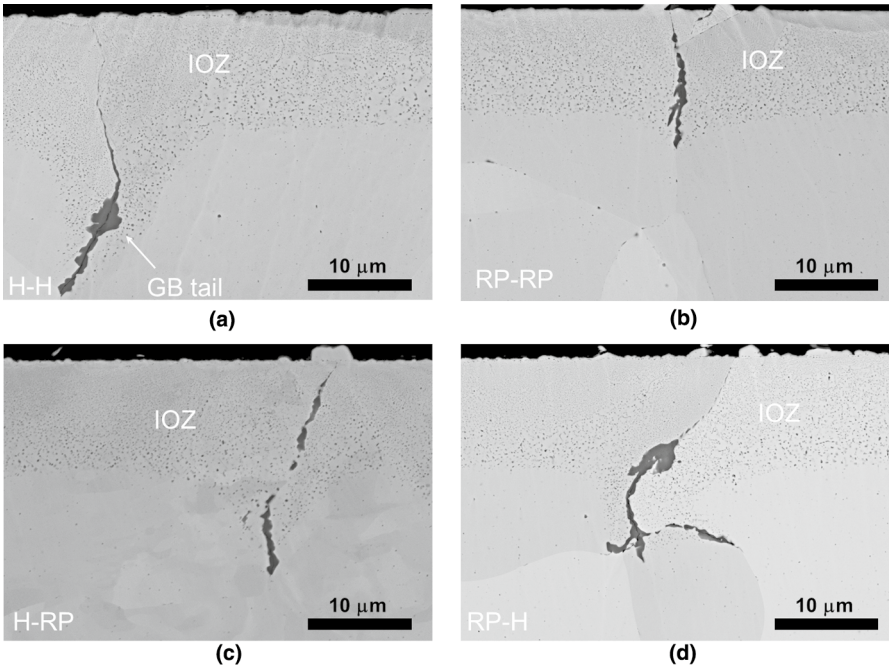


**Fig. 9** BSE images of internal oxidation zones IOZ in BIB cross-sectioned Fe–2.25Cr specimens alternatively exposed for 72 and 120 h at 700 °C in **a** RP and RP, **b** $H_2/H_2O$ and $H_2/H_2O$, **c** $H_2/H_2O$ and RP, **d** RP and $H_2/H_2O$

or $TiO_2$ were formed underneath an external chromia scale during parallel exposures in air and $H_2/H_2O$ [49, 50] or even in dual atmosphere conditions [12].

The present study fully corroborates the latter view. The bulk IOZs observed in both RP and $H_2/H_2O$ were equally broad (Figs. 2, 3c, d, 4). The calculated $N_O^{(s)}D_O$ values agreed well with the available literature data and revealed no significant effect of hydrogen. However, another important hydrogen effect was found in this study, i.e., the GB tail. In $H_2/H_2O$, the oxidation attack is deeper at alloy grain boundaries (Fig. 3a, b). This effect was observed after all exposure times at 700 °C but not at 800 °C and above. The total average penetration depth of the GB tail measured from the surface was a triple of the bulk IOZ at 700 °C (Fig. 3a) and is expected to be even stronger at lower temperatures while still measurable in a reasonable time-span. After all, hydrogen does have an effect on internal oxidation in Fe–Cr but not on the lattice oxygen permeability in iron: the effect is rather limited to intergranular oxidation. Possible interpretations of the GB tail will be discussed in the next section.

## Effect of Dual Atmosphere

The dual atmosphere gained widespread attention in the context of SOFC almost two decades ago [10] and has been extensively explored ever since [11–17]. Although

many mechanistical aspects of the dual atmosphere effect are not completely understood, a number of firm experimental facts were established: (i) hydrogen from the fuel side dissolves in the steel, migrates to the air side and disrupts protective scaling of $Cr_2O_3$ [13, 17]; (ii) the dual atmosphere effect diminishes with increasing temperature being most intense at 600 °C [14]; (iii) Cr evaporation on the air side may additionally undermine the protectiveness; however, it is not the primary reason of the effect occurring also on the dry air side [14]; (iv) cold-work [51–53] such as, e.g., grinding of the air side suppresses the dual atmosphere effect. The combination of (ii) and (iv) suggests that the dual atmosphere effect is related to Cr diffusion.

Among numerous mechanistic hypotheses, the hypothesis of an acceleration of inward oxygen transport by dissolved hydrogen [36] was discussed as one of possible explanations [13, 14]. However, the recent experimental evidence [42, 44, 48] as well as the internal oxidation results in the present study (Fig. 4) suggests no such effect, i.e., the lattice oxygen permeability is equal in both dry and humid exposures. The latter conclusion was confirmed by an actual dual atmosphere exposure in which the "dry" RP side was not in contact with any hydrogen bearing species, i.e., $H_2$ and $H_2O$, while the "humid" $H_2/H_2O$ side was an exclusive source of hydrogen dissolved in the alloy (Fig. 1a). As can be seen from Fig. 5 and Table 3, the bulk IOZs measuring $10.6 \pm 1$ µm (RP side) and $11.0 \pm 1$ ($H_2/H_2O$ side) µm in width were not affected by the dual atmosphere. Furthermore, the grain boundary tails did not evolve as they did on the $H_2/H_2O$ side. The internal oxidation morphologies obtained in the dual atmosphere experiment essentially recapitulated the single-exposure microstructural pattern.

Two important conclusions can be drawn from this observation:

(i) dual atmosphere conditions and, hence, dissolved hydrogen do not affect lattice oxygen permeability in ferrite and thus do not accelerate internal oxidation.
(ii) hydrogen dissolved in the alloy is not responsible for the intergranular oxidation attack observed in the single $H_2/H_2O$ exposures (Fig. 3) as well as on the $H_2/H_2O$ side of the dual atmosphere specimen at 700 °C (Fig. 5).

This finding thus points at the $H_2/H_2O$ atmosphere as the trigger of the intensified grain boundary attack in the IOZ at 700 °C. The role of $H_2O$ needs to be further studied to better understand a higher susceptibility of alloy grain boundaries to internal oxidation attack at lower temperature in $H_2/H_2O$.

### Intergranular oxidation attack

The most puzzling finding in the present study was the intergranular oxidation attack promoted by the $H_2/H_2O$-environment (Figs. 3a, 5a). GB tails or intergranular internal oxidation has been previously reported by Auinger et al. [54, 55] and Ronqueti et al. [56] for diluted (0.2–1 wt.%) binary Fe–Cr, Fe–Al, Fe–Si and Fe–Mn alloys exposed in humidified Ar-$H_2$ or $N_2$-$H_2$ gas mixtures below FeO formation at 600–700 °C. Intergranular tails were found in Fe–Cr and Fe–Si but not in Fe–Al and Fe–Mn [54, 55], while the pattern became more complex in ternary model alloys.

Despite slight differences in Cr concentration (0.8 wt.% in [55]) and hydrogen pressure (25 mbar in [55]), the ratio between GB tail penetration and bulk IOZ width, $X_{IG}/X_{IOZ}$, found in [55] is 2.6 which is in excellent accord with the value 2.9 obtained in the present study. The $X_{IG}/X_{IOZ}$, ratio is expected to increase with decreasing temperature [56]. While these data independently confirm the enhanced intergranular attack in $H_2/H_2O$ for diluted Fe–Cr alloys observed in the present study, the role of alloy chemistry, grain size and especially that of humidity remains obscure.

The easiest and intuitive way to interpret enhanced intergranular oxidation in $H_2/H_2O$ would be to ascribe it to the hydrogen dissolved in the alloy. In addition, such a role of hydrogen would be an elegant alternative explanation for the dual atmosphere effect, i.e., although hydrogen has no effect on bulk oxygen permeability (Figs. 2, 3, 4, 5) it accelerates oxygen ingress at grain boundaries. However, the experimental evidence does not support this hypothesis. The RP—$H_2/H_2O$ dual exposure (Fig. 6) revealed absolutely no effect of dual atmosphere, i.e., dissolved hydrogen, on the evolution of intergranular oxidation. On the RP side, the GB tails did not develop much beyond the bulk IOZ, while those on the $H_2/H_2O$ side reproduced a single atmosphere IOZ morphology typical for the $H_2/H_2O$ exposures at 700 °C.

To better understand the role of hydrogen in the intergranular oxidation attack, a series of exposures were carried out in RP with an increasing pressure of Ar–5%$H_2$. The residual Ar–5%$H_2$ pressure was set to attain 1, 2 and 3 bar total pressure at 700 °C. The corresponding $pH_2$ and $pH_2O$ can be calculated from a thermodynamic equilibrium of reaction

$$H_2(g) + FeO(s) = H_2O(g) + Fe(s) \quad (1)$$

Taking the standard enthalpies and entropies from [57], calculating the equilibrium constant $K_p$, one arrives at a ratio $\frac{pH_2}{pH_2O} = 2.73$ to maintain the $pO_2$ in the system at the Fe/FeO level buffered by the RP. The equilibrium (1) does not depend on the total pressure. Hence, the partial pressures of $H_2O$ and $H_2$ in the pressurized experiments were 36.6/13.4 (at 1 bar), 73.2/26.8 (at 2 bar) and 109.8/40.2 (at 3 bar). A very similar experiment was conducted in [39, 40] where no oxidation at the GB was reported. In the present study, no detectable effect of $pH_2$ on the bulk IOZ could be established (Fig. 8). On the other hand, only a weak increase of intergranular oxidation was measured in the pressurized capsules (Fig. 8). Nevertheless, the GB tails had a much lower penetration depth compared to the IOZs obtained under the flowing $H_2/H_2O$. A plausible explanation for this observation could be a limited availability of the hydrogen bearing species compared to the flowing Ar-$H_2$-$H_2O$ gas mixture.

The alternated exposures in Fig. 9 clearly demonstrated that the penetration depth of the intergranular oxidation attack correlates with the time of exposure to the $H_2/H_2O$ environment. For instance, the intergranular oxidation depth after 72 h in $H_2/H_2O$ at 700 °C was $22.1 \pm 1$ µm, while the tail length of $20.6 \pm 2$ µm was measured in the specimen exposed for 72 h in $H_2/H_2O$ and subsequently reacted in RP for another 120 h at 700 °C (Fig. 9c and Table 3). In other words, the GB tail ceased to propagate once the $H_2/H_2O$ atmosphere was switched off, while the bulk IOZ kept on growing as if the exposure was uninterrupted. The data presented above suggest

absolutely no effect of hydrogen dissolved in the metal on the intergranular internal oxidation. Neither the source of hydrogen, i.e., dual atmosphere or gaseous hydrogen equilibrated with Fe/FeO, plays any significant role. Thus, only $H_2O$ in the gas can be considered as the trigger of the intergranular attack.

A very similar corrosion phenomenon is well known to occur in nuclear materials exposed to pressurized water reactor (PWR) primary water environment: intergranular stress corrosion cracking (IGSCC). For the first time reported for 304 and 347 steel pipes in the 1960s [58], IGSCC was later observed also in Ni-based alloys [59] such as alloy 600 [60–62]. It is generally accepted that IGSCC is the caused by internal oxidation [63]. Despite great progress in experimental and theoretical exploration of this effect even on the atomistic level [64–66], the actual role of the $H_2O$ molecule is still not fully understood.

Furthermore, the internal oxidation model is still being questioned [67] as the IGSCC propagation rates exceed by four orders of magnitude any available bulk oxygen permeability [68] or Cr diffusivity data [69–71] extrapolated to 350–400 °C. The latter is not surprising as grain boundary transport mechanisms should prevail at such lower temperature while most oxygen permeability datasets were measured accounting exclusively for lattice transport. IGSCC is also simulated in an accelerated corrosion tests in superheated hydrogenated steam, i.e., $H_2/H_2O$ gases [62].

Given all morphological similarities between IGSCC and the GB attack observed in the present study, one should bear in that these phenomena are not the same as SCC requires three key factors: environment, susceptible microstructure, and stress. Only the first one is relevant for intergranular attack induced by the $H_2/H_2O$ gas in the presented model experiments (Fig. 3). Furthermore, the key role of water in grain boundary oxidation attack at lower temperatures (700 °C and below), the nature of the species entering a GB and acting as an oxidant, the role of dissolved hydrogen and other factors need to be further explored to gain a better mechanistic understanding of this phenomenon.

## Conclusions

The following conclusions can be drawn from this study:

- Hydrogen has no effect on alloy lattice oxygen permeability in Fe–Cr in the SOFC/SOEC relevant temperature range of 700–900 °C.
- $H_2/H_2O$ does affect the internal oxidation in Fe–Cr but only at temperatures below 800 °C provoking an increased oxidation attack at alloy grain boundaries (GB) propagating beyond the bulk IOZ
- The GB oxidation attack is most likely caused by water from the $H_2/H_2O$ gas.
- Dual atmosphere conditions do not change the internal oxidation pattern of Fe–Cr. Both RP and $H_2/H_2O$ sides reveal an identical IOZ morphology compared to the respective single exposure counterparts.
- Hydrogen dissolved in the alloy does not induce the GB oxidation attack as the RP side in the dual atmosphere experiment did not develop any GB tails.

**Acknowledgements** Funding was provided by the Swedish Energy Agency (Grant: 2015-009652).

**Funding** Open access funding provided by Chalmers University of Technology.



## References

1. A. B. Stambouli and E. Traversa, *Renewable and Sustainable Energy Reviews* **6**, 433 (2002).
2. Y. Zheng, J. Wang, B. Yu, et al., *Chemical Society Reviews* **46**, 1427 (2017).
3. A. Hauch, R. Küngas, P. Blennow, et al., *Science* **2020**, 370 (1979).
4. K. Chen and S. P. Jiang, *Journal of The Electrochemical Society* **163**, F3070 (2016).
5. A. Nechache and S. Hody, *Renewable and Sustainable Energy Reviews* **149**, 2021 111322.
6. W. J. Quadakkers, J. Piron-Abellan, V. Shemet, and L. Singheiser, *Materials at High Temperatures* **20**, 115 (2003).
7. S. Chevalier, L. Combemale, I. Popa, et al., *Solid State Phenomena* **300**, 135 (2020).
8. M. Stanislowski, J. Froitzheim, L. Niewolak, et al., *Journal of Power Sources* **164**, 578 (2007).
9. C. Goebel, R. Berger, C. Bernuy-Lopez, J. Westlinder, J. E. Svensson, and J. Froitzheim, *Journal of Power Sources* **449**, 2020 227480.
10. Z. Yang, M. S. Walker, P. Singh, and J. W. Stevenson, *Electrochemical and Solid-State Letters* **6**, B35 (2003).
11. G. R. Holcomb, M. Ziomek-Horoz, S. D. Cramer, B. S. Covino, and S. J. Bullard, *Journal of Materials Engineering and Performance* **15**, 404 (2006).
12. A. W. Bredvei Skilbred and R. Haugsrud, *International Journal of Hydrogen Energy* **37**, 8095 (2012).
13. P. Alnegren, M. Sattari, J. E. Svensson, and J. Froitzheim, *Journal of Power Sources* **301**, 170 (2016).
14. P. Alnegren, M. Sattari, J. E. Svensson, and J. Froitzheim, *Journal of Power Sources* **392**, 129 (2018).
15. K. Chandra and A. Kranzmann, *Corrosion Engineering Science and Technology* **53**, 27 (2018).
16. C. Goebel, P. Alnegren, R. Faust, J. E. Svensson, and J. Froitzheim, *International Journal of Hydrogen Energy* **43**, 14665 (2018).
17. K. O. Gunduz, A. Chyrkin, C. Goebel, et al., *Corrosion Science* **179**, 2021 109112.
18. A. Chyrkin, K. O. Gunduz, V. Asokan, J.-E. Svensson, and J. Froitzheim, *Corrosion Science* **203**, 2022 110338.
19. E. Essuman, G. H. Meier, J. Żurek, M. Hänsel, and W. J. Quadakkers, *Oxidation of Metals* **69**, 143 (2008).
20. B. Pujilaksono, T. Jonsson, H. Heidari, M. Halvarsson, J. E. Svensson, and L. G. Johansson, *Oxidation of Metals* **75**, 183 (2011).
21. G. H. Meier, K. Jung, N. Mu, et al., *Oxidation of Metals* **74**, 319 (2010).
22. D. J. Young, J. Zurek, L. Singheiser, and W. J. Quadakkers, *Corrosion Science* **53**, 2131 (2011).
23. J. Zurek, E. Wessel, L. Niewolak, et al., *Corrosion Science* **46**, 2301 (2004).
24. H. Asteman, J. E. Svensson, and L. G. Johansson, *Oxidation of Metals* **57**, 193 (2002).
25. H. Asteman, J. E. Svensson, M. Norell, and L. G. Johansson, *Oxidation of Metals* **54**, 11 (2000).
26. D. J. Young and B. A. Pint, *Oxidation of Metals* **66**, 137 (2006).
27. G. R. Holcomb, *Oxidation of Metals* **69**, 163 (2008).
28. B. Tveten, G. Hultquist, and T. Norby, *Oxidation of Metals* **51**, 221 (1999).

29. Norby T. Le, *Journal de Physique IV* **3**, C9-99 (1993).
30. J. Ehlers, D. J. Young, E. J. Smaardijk, et al., *Corrosion Science* **48**, 3428 (2006).
31. E. Essuman, G. H. Meier, J. Zurek, M. Hänsel, L. Singheiser, and W. J. Quadakkers, *High Temperature Corrosion and Protection of Materials 7, Pts 1 and 2* **595–598**, 699 (2008).
32. E. Essuman, L. R. Walker, J. Maziasz, and B. A. Pint, *Materials Science and Technology* **29**, 822 (2013).
33. E. Essuman, G. H. Meier, J. Zurek, et al., *Journal of Materials Science* **43**, 5591 (2008).
34. A. Rahmel and J. Tobolski, *Corrosion Science* **5**, 815 (1965).
35. C. T. Fujii and R. A. Meussner, *Journal of The Electrochemical Society* **111**, 1215 (1964).
36. E. Essuman, G. H. Meier, J. Zurek, M. Hänsel, L. Singheiser, and W. J. Quadakkers, *Scripta Materialia* **57**, 845 (2007).
37. W. J. Quadakkers, J. Żurek, and M. Hänsel, *JOM* **61**, 44 (2009).
38. J. Zurek, G. H. Meier, E. Wessel, L. Singheiser, and W. J. Quadakkers, *Materials and Corrosion* **62**, 504 (2011).
39. A. R. Setiawan, M. Hanafi Bin Ani, M. Ueda, K. Kawamura, and T. Maruyama, *ISIJ International* **50**, 259 (2010).
40. M. H. B. Ani, T. Kodama, M. Ueda, K. Kawamura, and T. Maruyama, *Materials Transactions* **50**, 2656 (2009).
41. D. Jullian, J. Zhang, D. B. Hibbert, and D. J. Young, *Journal of Alloys and Compounds* **732**, 646 (2018).
42. A. Prillieux, D. Jullian, J. Zhang, D. Monceau, and D. J. Young, *Oxidation of Metals* **87**, 273 (2017).
43. P. Guo, J. Zhang, D. J. Young, and C. H. Konrad, *Oxidation of Metals* **83**, 223 (2015).
44. V. Shemet and M. Hänsel, *Materials Letters* **172**, 6 (2016).
45. A. Chyrkin, C. Cossu, J. Froitzheim, and J.-E. Svensson, *Oxidation of Metals* **97**, 527 (2022).
46. J. Takada, K. Kashiwagi, and M. Adachi, *Journal of Materials Science* **19**, 3451 (1984).
47. J. Takada, S. Yamamoto, S. Kikuchi, and M. Adachi, *Oxidation of Metals* **25**, 93 (1986).
48. D. Jullian, A. Prillieux, J. Zhang, and D. J. Young, *Materials and Corrosion* **68**, 197 (2017).
49. J. P. Abelián, *ECS Proceedings Volumes* **16**, 811 (2001).
50. A. Chyrkin, P. Huczkowski, V. Shemet, L. Singheiser, and W. J. Quadakkers, *Oxidation of Metals* **75**, 143 (2011).
51. D. Caplan and M. Cohen, *Corrosion Science* **6**, 321 (1966).
52. S. Leistikow, I. Wolf, and H. J. Grabke, *Werkstoffe und Korrosion* **38**, 556 (1987).
53. C. Ostwald and H. J. Grabke, *Corrosion Science* **46**, 1113 (2004).
54. M. Auinger, E. M. Müller-Lorenz, and M. Rohwerder, *Corrosion Science* **90**, 503 (2015).
55. M. Auinger, V. G. Praig, B. Linder, and H. Danninger, *Corrosion Science* **96**, 133 (2015).
56. L. A. Ronqueti, J. Favergeon, M. Risbet, and M. Picard M, Study of grain boundary oxidation of high alloyed carbon steels at coiling temperature, in *53rd Rolling Seminar* (2017), p. 283. https://doi.org/10.5151/1983-4764-27735.
57. I. Barin, F. Sauert, E. Schultze-Rhonhof, and W. S. Sheng, *Thermochemical Data of Pure Substances, Part 1, Ag-Kr*, (VCH, 1993).
58. F. P. Ford, B. M. Gordon, and R. M. Horn, *Intergranular stress corrosion cracking (IGSCC) in boiling water reactors (BWRs). Nuclear Corrosion Science and Engineering*, (Woodhead Publishing Limited, 2012). https://doi.org/10.1533/9780857095343.5.548.
59. B. M. Capell and G. S. Was, *Metallurgical and Materials Transactions A: Physical Metallurgy and Materials Science* **38**, 1244 (2007).
60. G. Bertali, F. Scenini, and M. G. Burke, *Corrosion Science* **114**, 112 (2017).
61. G. Bertali, M. G. Burke, F. Scenini, and N. Huin, *Metallurgical and Materials Transactions A: Physical Metallurgy and Materials Science* **49**, 1879 (2018).
62. L. Volpe, M. G. Burke, and F. Scenini, *Acta Materialia* **175**, 238 (2019).
63. T. S. Gendron, P. M. Scott, S. M. Bruemmer, and L. E. Thomas, in *Internal Oxidation as a Mechanism for Steam Generator Tube Degradation* (Canada, 1999).
64. L. Luo, M. Su, P. Yan, et al., *Nature Materials* **17**, 514 (2018).
65. L. Luo, L. Li, D. K. Schreiber, et al., *Science Advances* **6**, 1 (2020).
66. S. M. Bruemmer, M. J. Olszta, M. B. Toloczko, and D. K. Schreiber, *Corrosion Science* **131**, 310 (2018).
67. R. W. Staehle, Assessment of internal oxidation (IO) as a mechanism for submodes of stress corrosion cracking that occur on the secondary side of steam generators, in *Miner. Met. Mater. Soc. Prep.*

*Div. Eng. Technol. Off. Nucl. Regul. Res. U.S. Nucl. Regul. Comm. Washington, DC 20555-0001 NRC Job Code W6588 NUREG/CR-6827 RWS 154* (2004).
68. J. W. Park and C. J. Altstetter, *Metallurgical Transactions A* **18**, 43 (1987).
69. T. Gheno, F. Jomard, C. Desgranges, and L. Martinelli, *Materialia (Oxf)* **3**, 145 (2018).
70. T. Gheno, F. Jomard, C. Desgranges, and L. Martinelli, *Materialia (Oxf)* **6**, 100283 (2019) .
71. S. P. Murarka, M. S. Anand, and R. P. Agarwala, *Journal of Applied Physics* **35**, 1339 (1964).